Internal-Wave Energy Fluxes on the New Jersey Shelf

ZACHARIAH R. HALLOCK AND ROBERT L. FIELD

Naval Research Laboratory, Stennis Space Center, Mississippi

(Manuscript received 1 December 2003, in final form 7 June 2004)

ABSTRACT

Internal-wave energetics derived from moored acoustic Doppler current profiler (ADCP) observations on the New Jersey shelf are described. Horizontal and vertical velocity components from three 40-day ADCP records acquired near the shelf edge south of the Hudson Canyon were bandpass filtered to isolate high-frequency internal waves. In this band (0.5–7.5 h^{-1}) the vertical component of velocity is significant and is integrated to yield elevation anomaly. Using the ADCP data with buoyancy frequency profiles from nearby CTD station data, kinetic energy (KE), baroclinic potential energy (PE), and energy flux were calculated. Results show depth-averaged KE and PE are nearly equal and of order 10^{-3} J kg^{-1}, and there are significant northwestward fluxes, generally parallel to the bathymetry gradient, during most of the record, with depth-integrated magnitudes sometimes exceeding 100 W m^{-1}. Vertical energy fluxes are small relative to horizontal fluxes. Vertical profiles of time-averaged flux suggest a dominant first internal-wave mode. Depth-integrated, time-averaged fluxes range from 9 to 24 W m^{-1}, with the highest values occurring 18 km southwest of the Hudson Canyon. Two-dimensional probability density functions are estimated for energy flux. Group velocity of a large-amplitude internal-wave packet is estimated at 0.36 m s^{-1}.

1. Introduction

Internal tides and supertidal internal waves are ubiquitous features in many shelf regions. These processes are often excited by interaction of the barotropic tide with shelf topography (Colosi et al. 2001; Baines 1982; Holloway et al. 2001). Where the interaction is with the shelf break, the waves generally propagate shoreward, their properties changing as water depth decreases. Internal waves excited in this way are often of large amplitude and nonlinear, forming packets of solitons (Inall et al. 2001; Holloway et al. 2001, 1997; Holloway 1987; Small et al. 1999; Hallock et al. 2000). The ability to estimate propagation characteristics of these phenomena is important in understanding fluctuations in acoustic transmissions, as described by Field et al. (2003, manuscript submitted to *IEEE J. Ocean Eng.*) and Apel et al. (1997). Some have found it useful to calculate the baroclinic energy flux associated with internal waves to provide (for example) estimates of energy available for mixing and dissipation. Recent estimates of depth-integrated internal tidal energy fluxes along the Hawaiian Ridge (Rudnick et al. 2003) range from 1.3 to 39 kW m^{-1}. By comparison, Alford (2003) reports fluxes in the semidiurnal and inertial bands at locations around the globe that range from about 1 to 20 kW m^{-1}. A similar result was found by Althaus et al. (2003) at the Mendocino Escarpment. Here, semidiurnal internal tidal fluxes of order 5 kW m^{-1} directed away from the escarpment (northward and southward) were found. Along the shelf edge of the eastern United States these estimates are lower than elsewhere, of the order of 1 kW m^{-1} or less. In these studies fluxes are generally directed from the topographic generation toward deeper water where dissipation and mixing may result. On the other hand, Kunze et al. (2002) find generally upslope energy fluxes in the Monterrey Canyon for internal tides at semidiurnal and higher harmonic frequencies, diminishing from 5 to about 1 kW m^{-1}. Previous studies have relied on concurrent measurements of horizontal current profiles and vertical displacement of isopycnals to calculate energy flux. This is necessary for lower-frequency internal waves (tidal, inertial, etc.), where direct measurements of vertical velocity are inaccurate. Here, in contrast, we use horizontal and vertical velocities measured by moored acoustic Doppler current profilers (ADCPs) to derive kinetic energy fluxes, as well as kinetic and potential energies of internal waves in the frequency band between 0.5 cph and the Nyquist limit 7.5 cph. These results compare favorably with nearby measurements presented by MacKinnon and Gregg (2002, henceforth MG).

The data used in this study consist of three, 40-day-long moored ADCP records from near the shelf edge, east of New Jersey and south of the Hudson Canyon. Other supporting data include CTD stations (single and repeated) and a moored temperature chain. The focus

Corresponding author address: Dr. Zachariah R. Hallock, 2618 Lebanon Road, Efland, NC 27243.
E-mail: zack.hallock@southwind.org

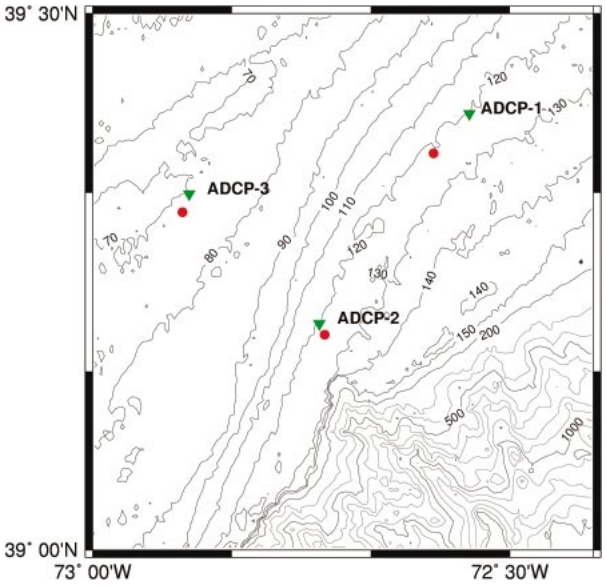

FIG. 1. Locations of moored ADCPs (green triangles) and secondary CTD stations (red circles); initial CTD stations were within 100 m of the ADCP sites. The bathymetry is from the National Oceanic and Atmospheric Administration (NOAA) National Geophysical Data Center (NGDC) high-resolution database.

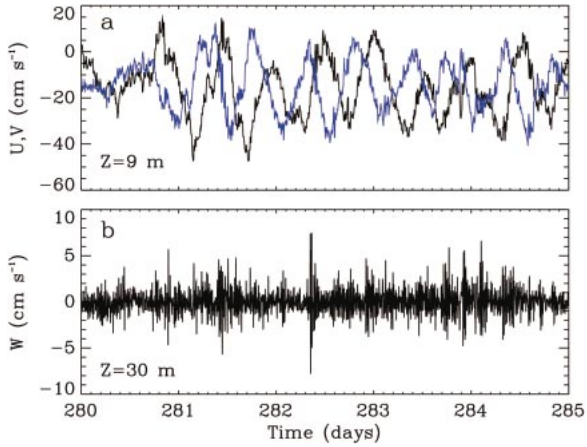

FIG. 2. Five-day sample of current velocity components from ADCP 3: (a) eastward (*U*, black) and northward (*V*, blue) at 9 m and (b) upward (*W*) at 30 m.

here is on the ADCP data. Section 2 is a description of data used, section 3 describes analysis methods, section 4 is a discussion of results, and conclusions are presented in section 5.

2. Observations

In autumn 2000 an extensive set of oceanographic measurements was made by investigators from the Naval Research Laboratory (NRL) in a region of the Mid-Atlantic Bight near 39.3°N, 72.7°W (Fig. 1). The observations were made in support of the U.S.–Japan Shallow Water Acoustic Technology (SWAT) experiment. Positions of moored ADCPs (deployed from 30 September to 7 November 2000) appear in Fig. 1. CTD stations were conducted at and near the positions of the ADCPs at various times during the ADCP deployment.

a. ADCP data

The ADCPs were 307.2-kHz broadband ''Workhorse Sentinels'' manufactured by RD Instruments. The ADCPs were deployed in trawl-resistant mounts that were lowered (rather than free-dropped) to the bottom and positioned so as to minimize tilt of the transducer head from the (ideal) vertical orientation. The vertical bin size was 2 m for ADCPs 1 and 2 and 1 m for ADCP 3; valid current measurements were acquired from about 10 m beneath the surface to about 4 m above the bottom. Close to the surface, velocity data were contaminated by sidelobe interference, while near the bottom a blanking distance of about 2.7 m from the transducer adds to the ~1-m height of the instrument. Water depths at the moorings ranged from 75 to 120 m. The sampling scheme used was a 1-min burst of 120 samples, repeated at 4-min intervals, giving a sampling interval of 4 min. Burst sampling was used to minimize aliasing of the measurement by high-frequency surface gravity waves. Velocity data from each sample were resolved into vertical, northward, and eastward components, corrected for residual sensor tilt using measured pitch and roll angles, and then averaged over the burst. Velocities were rotated to correct for local magnetic variation. The sample (burst average) velocity uncertainty is estimated to be 1.5 cm s^{-1} or less. Figure 2 shows a portion of the velocity time series from ADCP 3. The horizontal velocity (*U*, *V*; Fig. 2a) contains a strong tidal/inertial signal as well as longer periods and supertidal fluctuations. The average velocity for the data shown in the figure (and over the entire record) is southwestward, generally along isobaths. The vertical velocity (*W*) appears to be more band-limited and is dominated by bursts of supertidal variability. Longer-period signals are present but are close to the noise floor of the instrument. Coherences between vertical and horizontal velocity (not shown) are negligible, ruling out contamination of the former resulting from sensor inclination.

b. CTD data: Buoyancy frequency profiles

Short repeated CTD casts (each set of 5–10 taking about 1 h) were done at all three ADCP locations at the times of deployment. Other CTD stations were conducted throughout the area later in the ADCP record. Three of these later casts, which were close to the ADCP sites, were selected (Fig. 1, red circles) to provide an estimate of hydrographic variability. Profiles of buoyancy frequency (*N*) (Fig. 3) are based on averages of the short, initial CTD series (black) and on selected single casts acquired later (green), yielding two reali-

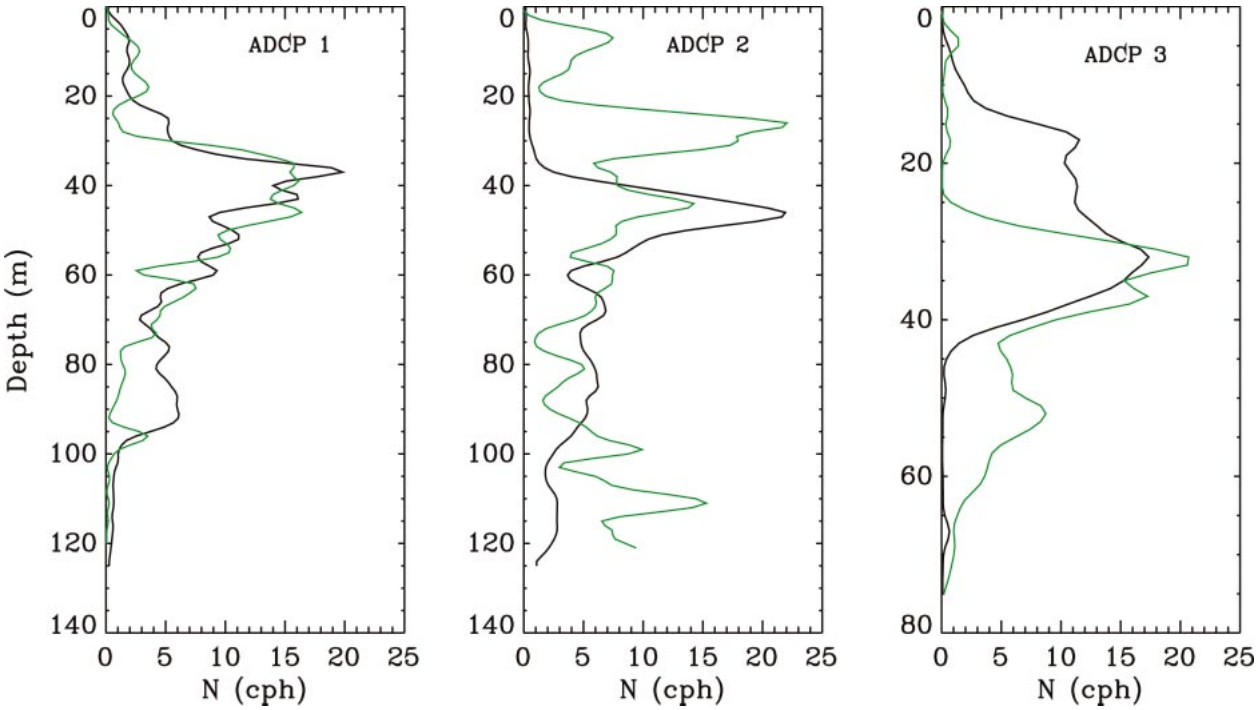

FIG. 3. Buoyancy frequency (N) profiles at ADCPs 1–3 from averages of short, initial yo-yo CTD casts (black) and from casts conducted later in the ADCP records (green).

zations at each ADCP location. Temporal and spatial variability of N is pronounced in this region; note in particular the secondary maximum near 100 m at ADCP 2 for the later CTD cast (green), which is associated with an intrusion of slope water. We use the two profiles for each location to provide a rudimentary estimate of uncertainty in subsequent calculations.

c. Moored temperature chain

A moored chain consisting of 10 (first deployment) and 14 (second deployment) temperature recorders with vertical separation across the thermocline of 5 m was deployed, about 200 m from ADCP 3, for 6 days near the beginning of the ADCP record and again for 14 days near the end. Strong temperature/salinity (T/S) variability associated with fronts posed some difficulties identifying internal-wave signatures in the temperature data, but, where it was possible, thermocline height anomaly was calculated for comparison with ADCP-derived elevations (below).

3. Analysis

a. Spectra

Autospectra for eastward velocity near the surface (Fig. 4a) show semidiurnal tidal peaks with a change in slope beginning near 20 cycles per day (cpd). Spectra for northward velocities (not shown) are quite similar. Spectral energy for vertical velocity (Fig. 4b) shows a broad maximum between about 20 and 100 cpd. These spectra are averages of sample spectra calculated on 2-day segments. To better estimate amplitudes of short internal-wave bursts, spectra for vertical velocity were recalculated using 2-h segments. For the 2-h sample spectra, the band from 1.5 to 4.5 cycles per hour (cph) contains most of the variance; the center of this band corresponds to a period of about 20 min. For a small number of these segments, amplitudes reach several centimeters per second; about 3% exceed 2 cm s^{-1} for ADCPs 1 and 3 but only 0.5% for ADCP 2, where 1.3% exceed 1.5 cm s^{-1}. Even for 2-h segments, attenuation may result for wave packets whose amplitude changes significantly over that time. Amplitudes for lower frequencies (e.g., tidal) are well below the noise floor (about 1 cm s^{-1}) of the ADCP and hence are not usable in analyses. This makes intuitive sense if we consider a rather large (20-m amplitude) internal wave represented by isopycnal displacement at two periods: 12 and 0.5 h—that is, $\zeta = 20\cos(2\pi t/T)$, where T is the period. The time derivative yields W (vertical velocity) with amplitudes 0.2 and 9 cm s^{-1} for the respective periods above. We therefore focus on the band between 0.5 cph and the Nyquist limit, 7.5 cph (indicated by the vertical dashed lines in Fig. 4). Subsequent analyses were done using bandpass-filtered horizontal and vertical velocity data. Our results are therefore limited to this band.

b. Bandpassed velocity data

Integration of $W(z, t)$ in time yields vertical displacement $\zeta(z, t)$. This procedure was used successfully by

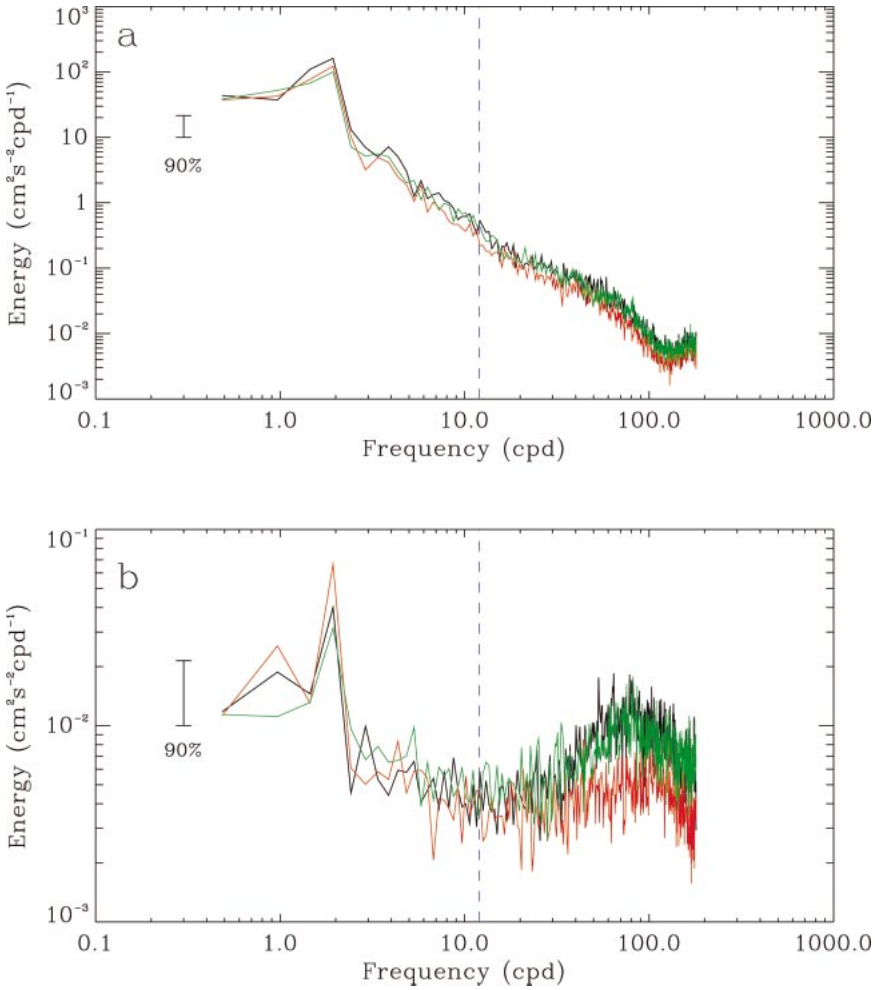

FIG. 4. Autospectra of (a) eastward (U) and (b) vertical (W) velocity components at ADCPs 1, 2, and 3 (black, red, and green). The 90% confidence limits are shown as error bars.

Inall et al. (2001) for frequencies at and above 1 cph. Amplification of low-frequency residuals (from the bandpass filtering) required trend removal after integration. The resulting elevations are used in the calculation of baroclinic pressure anomalies and potential energy. A 2.4-h segment of bandpass-filtered data from ADCP 3 (Fig. 5) shows a burst of internal-wave activity with a period of about 30 min (which is near the midpoint of the elevated energy band in Fig. 4b). The similar magnitudes and opposite phase (within the burst) of U and V (Fig. 5a) suggest wave propagation northwestward or southeastward; W is relatively high within such bursts (Fig. 5b), exceeding by at least an order of magnitude the amplitudes at lower frequencies. The nonstationary nature of these wave bursts, in both amplitude and phase, results in lower mean-square levels in the spectra of Fig. 4. The elevation (ζ; Fig. 5c) within the thermocline shows peak-to-peak excursions of nearly 25 m within the wave packet. The green curve in Fig. 5c represents the height of the 16° isotherm derived from the moored chain data (the chain data have been shifted by about 7 min to align the peaks/troughs; the time lag is partially explained by the horizontal mooring separation and partially by uncertainty in absolute time references). The agreement for the large wave packet is good. For a number of other cases in which amplitudes are large (>5 m) and periods are between 1 h and 20 min, agreement is fair to good. For periods shorter than about 15 min, marginal sampling by the ADCP (Δt = 4 min), coupled with smoothing implicit in the integration of W, attenuates the ADCP-derived ζ. For periods longer than 1.5 h, ζ is attenuated by the high-pass filter; in this range ζ is also less reliable, having been derived through integration of W with magnitudes near the noise threshold (as discussed above). Hence, we qualify our results as being limited to the frequency band stated. As a consequence, borelike features (e.g., part of a solibore signal) having time scales on the order of 2 h or longer are not accounted for in this analysis. However, trains of solitons and other internal-wave packets are adequately resolved. The propagation direction ambiguity for, for example, the half-cycle indicated by ver-

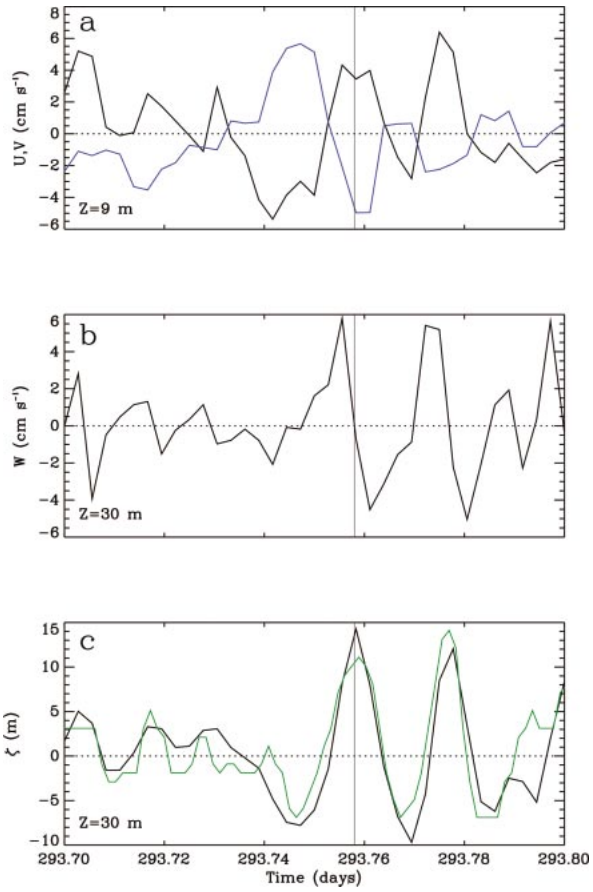

FIG. 5. Sample of bandpass-filtered (a) horizontal velocity (U, black; V, blue) at 9 m, (b) vertical velocity (W) at 30 m, and (c) elevation (ζ) calculated from W at 30 m, for a selected 0.1-day period, at ADCP 3. The green curve is thermocline height anomaly derived from moored-chain temperature data; it has been shifted in time by about 7 min to align the waves for comparison.

tical lines on the plot can be resolved (assuming dominance of the first baroclinic mode) by noting the positive (negative) correlation between $U(V)$ and ζ, implying it is roughly northwestward (Holt and Thorpe 1998). Calculation of baroclinic energy flux allows propagation direction determination without reference to modal structure.

c. Energy and energy flux

Total energy density (per unit mass) can be defined as

$$E \equiv \frac{\langle U^2 + V^2 \rangle_\varphi}{2} + \frac{\langle W^2 \rangle_\varphi}{2} + \frac{N^2 \langle \zeta^2 \rangle_\varphi}{2}$$

$$\equiv \mathrm{KE}_h + \mathrm{KE}_v + \mathrm{PE}, \quad (1)$$

where $\langle \rangle_\varphi$ indicates an average over phase ($\rho_0 E$ is energy per unit volume). In the case of these time series data this is accomplished by smoothing over 2 h, the longest period present in the bandpassed series. Horizontal and vertical energy flux are given by

$$\mathbf{F}_h = (\langle P'U \rangle_\varphi, \langle P'V \rangle_\varphi) \quad \text{and} \quad F_v = \langle P'W \rangle_\varphi, \quad (2)$$

where P' is the baroclinic pressure anomaly that can be derived from the elevation ζ and a relevant buoyancy frequency profile. Following Kunze et al. (2001),

$$\frac{P'(z, t)}{\rho_0} = \int_z^0 N^2(z')\zeta(z', t)\, dz' - \frac{1}{H}\int_{-H}^0 \int_z^0 N^2(z')\zeta(z', t)\, dz'\, dz. \quad (3)$$

The second term on the right is subtracted to satisfy the baroclinic condition of zero depth average pressure anomaly for free internal waves (Kunze et al. 2001). The expression (3) assumes hydrostatic balance, which may not be valid for frequencies close to N, in which case the time derivative of vertical velocity may be important. This was checked for these datasets and $\rho_0 \partial W/\partial t$ was found to be negligible relative to the $\partial P'/\partial z$ over most of the water column, except where both terms were near zero. Furthermore, effects errors in P' associated with the vertical acceleration become negligible for vertically integrated quantities.

Energies and fluxes [(1)–(3)] were calculated using ADCP horizontal velocities (U, V) and derived elevations (ζ) and buoyancy frequency profiles (N). We thus obtained two sets of E, $\mathbf{F}_h$, and F_v for each ADCP site, corresponding to the two sets of N profiles; the second set provides a rudimentary estimate of errors, and N affects potential energy and energy flux but not kinetic energy.

Mean (time averaged) profiles of energy density (Fig. 6a) show that PE and KE_h are comparable, but that KE_v is at least an order of magnitude less than KE_h. The vertical structure of PE reflects the stratification, and hence it decreases away from the pycnocline. There are significant differences between PE calculated with N profiles from the initial CTD casts (green, solid) and those from the later casts (dashed). Kinetic energy profiles, on the other hand, are relatively depth independent. The time dependence of depth-averaged energies for a 5-day segment of the three ADCP records (Fig. 7) also shows comparable magnitudes and correlation between PE (green) and KE_h (black), consistent with a wave process (note that quantities have been averaged over phase so that they constitute envelopes of the actual waveforms). Differences between depth-averaged PE series (green) and KE_h are also evident, particularly for ADCP 2, but they are not as pronounced as those in Fig. 6a. We note that while velocity magnitudes reported by MG are comparable to those in this study (Fig. 2), the depth-averaged energies in MG are 50–100 times ours, indicating that MG's results may actually be depth integrals; KE_v is also correlated but exhibits much lower magnitudes (Fig. 7 is typical of the entire record). Periods of higher energy are associated with internal-wave bursts or packets. The dominant direction of the horizontal flux vector $\mathbf{F}_h(z, t)$ is northwestward for the three

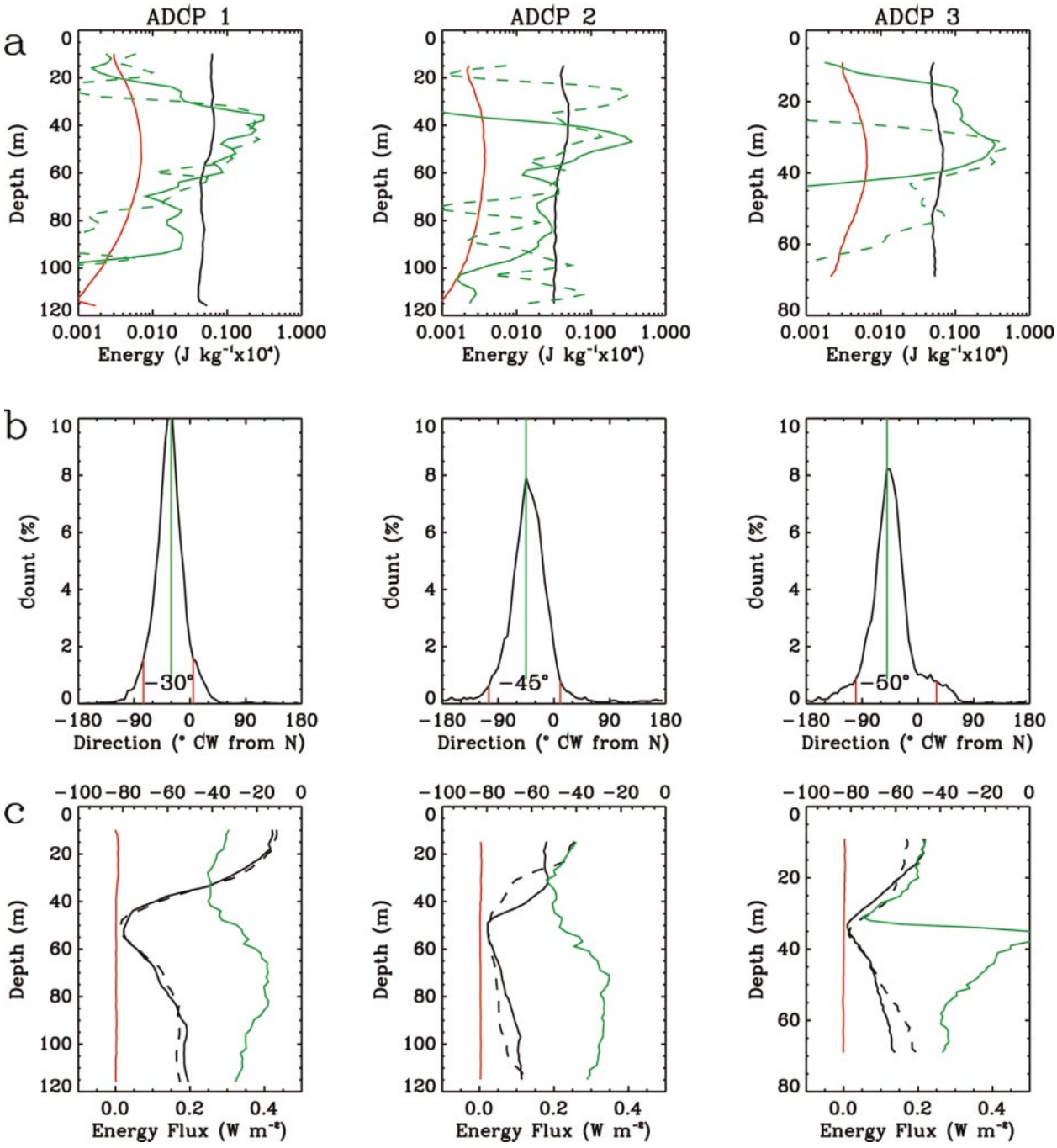

FIG. 6. (a) Profiles of time-averaged energy density of bandpassed ADCP data: horizontal (black) and vertical (red) kinetic energy; baroclinic potential energy (green). The abscissa is logarithmic. (b) Histograms of baroclinic horizontal energy flux direction. Data for which flux magnitudes fall below 0.05 of the record maximum are excluded. The green line denotes the direction of the histogram maximum and the red lines enclose 90% of the samples. (c) Profiles of time-averaged baroclinic energy flux: $|\overline{\mathbf{F}}_h|$ (black), direction of $\overline{\mathbf{F}}_h$ (green), and $\overline{F}_v$ (red). Dashed curves in (a) and (c) are based on the secondary N profiles.

ADCP locations (Fig. 6b), roughly upslope relative to local bathymetry. The histograms were constructed by selecting data samples for which the flux magnitude exceeded 5% of the maximum, thus avoiding errors introduced by spurious directions associated with magnitudes close to the noise level. The spread of directions is rather broad but 90% of the vectors fall within about $\pm 60°$ of the respective histogram maxima (red vertical lines). Directions of fluxes calculated using the later N profiles (not shown) are virtually the same as those

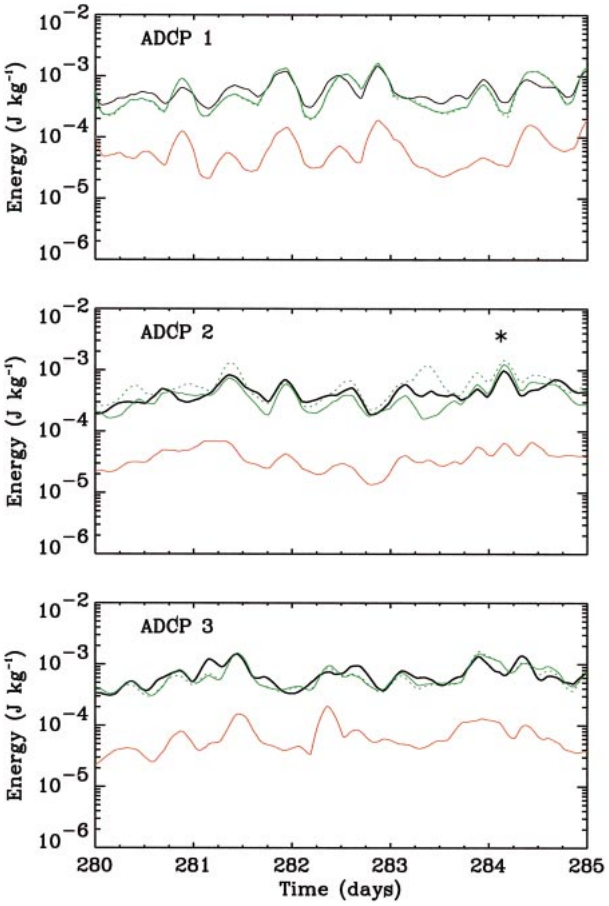

FIG. 7. The 5-day segment of depth-averaged kinetic and potential energy: KE_h (black), KE_v (red), and PE (green). The local maximum marked by an asterisk for ADCP 2 is used in an estimate of C_g. The dashed PE curves are based on the secondary N profiles.

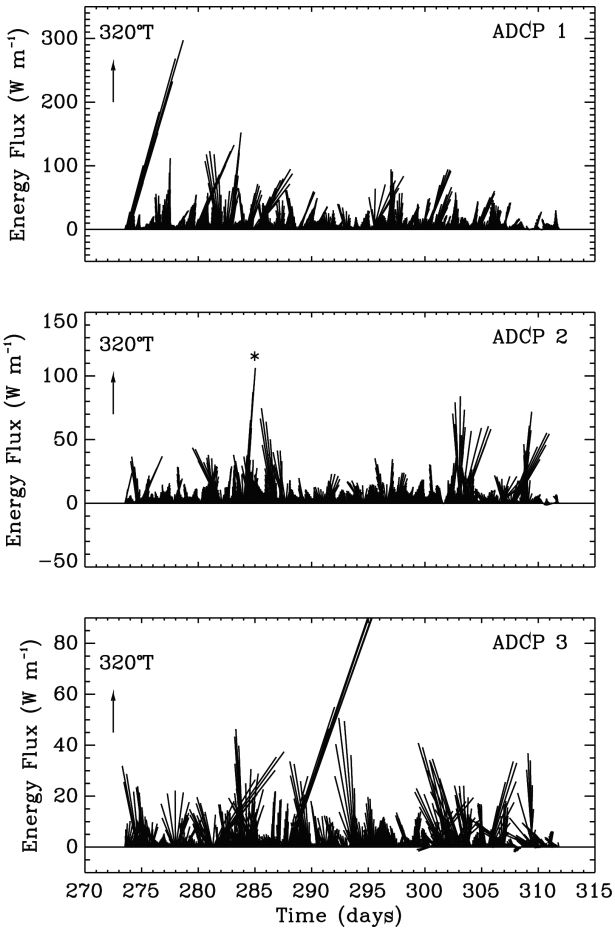

FIG. 8. Time series plots of $\hat{\mathbf{F}}_h$; vectors have been rotated so that the rotated y axis lies along 320°T. The vector marked by an asterisk for ADCP 2 is used in an estimate of C_g.

shown. Profiles of magnitudes (black) and directions (green) of time averages of $\mathbf{F}_h$ (Fig. 6c) show generally onshore fluxes with significant, but small, rotations with depth (as above, dashed profiles represent fluxes calculated with the later N profiles). The rotations, whose cause in unclear, are similar in magnitude and sense at all locations (more pronounced at ADCP 3). Time averages of vertical flux F_v (red) are much smaller than the horizontal flux $\mathbf{F}_h$; the ratio of vertical to horizontal flux magnitude is at most 0.08 and generally less than 0.04 (corresponding to departure from horizontal flux by about 2°). The shapes of the profiles are consistent with first-mode variability. On the other hand, the depth independence of KE_h (Fig. 6a) does not show the expected minimum near the thermocline indicative of first-mode dominance. However, amplitudes for ζ generally fall off more rapidly with mode number than they do for horizontal velocity, and the flux is calculated using ζ. This difference in amplitude falloff is consistent with linear internal-wave theory (Phillips 1977) in which, for constant N, the magnitude ratio of $\mathbf{F}_h$ to KE_h is inversely proportional to the square of the mode number. Time histories (not shown) of flux components also indicate that the vertical component is generally an order of magnitude less than the horizontal component.

Last, we vertically integrate (as distinct from vertical averages as calculated for Fig. 7) the horizontal flux vectors,

$$\hat{\mathbf{F}}_h(t) = \int_{-H}^{0} \mathbf{F}_h(z, t)\, dz. \tag{4}$$

Time series (stick plots) of $\hat{\mathbf{F}}_h(t)$, rotated so that the y axis lies along 320°T, are shown in Fig. 8 (note that ordinate scales are different). The overall onshore sense of the flux is evident. There is a negative trend in magnitude at ADCP 1 (even excluding the large events near day 275); this trend is not seen at the other locations.

Another statistical measure of the energy flux variability is a two-dimensional histogram (Fig. 9; histogram bin size is 1.0 W m^{-1}) providing a way to estimate the probability of finding the vector in a particular magnitude and direction interval. For example, the area sum of the fourth (northwest) quadrant of Fig. 9c (ADCP 3)

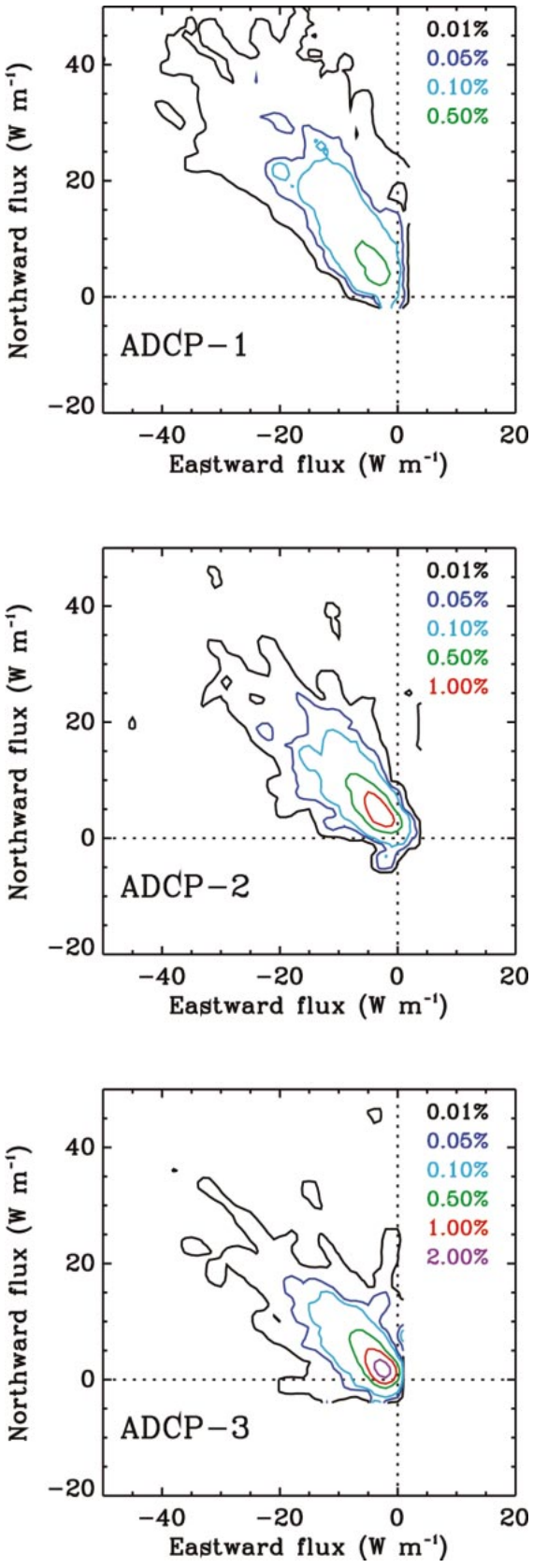

is 61.7% (excluding the zero bins; i.e., magnitude less than the bin size). The area integral of a histogram over a selected region, divided by $dx \times dy$ (the square of the bin size), yields the estimated probability that the flux vector will be found in the selected region. Figure 9 provides a compact summary of dominant energy flux and its variability.

4. Discussion

Figure 8 provides a time history of high-frequency propagating internal-wave events at three locations near the shelf edge. The more intense events are likely to be packets of solitons (e.g., Ostrovsky and Stepanyants 1989). Lower-magnitude fluxes may be associated with mixed solitary and dispersive waves. While propagation is consistently toward shallower water, there is considerable variability in direction suggesting different sources for wave packets, as suggested by MG. The characteristics of the fluxes depicted in Fig. 8 are quantitatively consistent with MG's results (their Fig. 14) where independent (of their ADCP data) determinations of elevation were used to calculate pressure anomalies.

Mean onshore, depth-integrated flux magnitudes at the three ADCP sites for the two sets of *N* profiles (Table 1) show a factor of 2 decrease from site 1 to 2 and a smaller decrease from 2 to 3. The latter (site 2 to 3; see Fig. 1) decrease could be interpreted as indicating dissipation as the wave groups travel shoreward. Also listed in the table are principal rms ellipses, indicating that variability is generally aligned with the mean vectors and has similar magnitudes. The results for the secondary *N* profiles (Table 1b) are similar to those using the initial *N* profiles; the largest difference is in the variance at ADCP 2, which is about 20 $W^2\ m^{-2}$ less. Following MG, using an average depth of 100 m, distance between ADCPs 2 and 3 of 18.5 km, average density of 1025 kg m^{-3}, and flux difference of $13.2 - 8.8 = 4.4$ W m^{-1}, we estimate dissipation at 2.3×10^{-9} W kg^{-1}. Using fluxes based on the secondary *N* profiles we get 1.7×10^{-9} W kg^{-1}, about 30% lower; the estimate is thus sensitive to changes in stratification. Furthermore, since the high-frequency internal waves (as defined here) may interact with lower-frequency waves (e.g., internal tides) and derive energy as they propagate, the problem may be more complex (MG). Also, since waves with periods on the order of 0.5 h have wavelengths of about 1 km (for the first mode and the local stratification) the packets are not coherent between the mooring sites and it is not clear where (between the sites) the apparent dissipation occurs; it might be spread out over

←

FIG. 9. Histograms of depth-integrated baroclinic energy flux at the ADCP locations. Histogram bin sizes (*dx, dy*) are 1 W m^{-1}. Contours are percent of total and are color keyed as shown; contour intervals are not equal.

TABLE 1. Time-averaged, depth-integrated fluxes, principal rms flux ellipses, and total variance. Based on initial N profiles.

	Magnitude (W m^{-1})	Direction (°T)	Major axis (W m^{-1})	Minor axis (W m^{-1})	Orientation (°T)	Variance (W^2 m^{-2})
(a)						
ADCP 1	24.4	−31	27.0	7.2	−64	779.5
ADCP 2	13.3	−39	12.8	4.1	−53	181.1
ADCP 3	8.8	−43	11.0	4.0	−61	136.7
(b)						
ADCP 1	24.5	−31	27.0	7.4	−64	785.2
ADCP 2	12.7	−41	11.7	3.7	−54	151.7
ADCP 3	9.4	−42	11.3	4.4	−59	146.5

the intervening distance (as hinted at by MG) or might be concentrated in regions where wave breaking or other nonlinear processes remove energy. Mackinnon and Gregg (2002) calculated a dissipation of 3×10^{-8} W kg^{-1}, more than 10 times our estimate, but most of the difference is explained by the different depths and distances used. This estimate of dissipation is based on time-averaged fluxes; values associated with individual internal-wave burst will be significantly higher. ADCP 1 was at the same isobath (120 m) as ADCP 2, and their mean flux levels differ by a factor of 2. A similar explanation cannot be used in this case since the dominant flux direction is perpendicular to the line connecting ADCPs 1 and 2.

The magnitudes of the fluxes found here are orders of magnitude less than the deep-ocean values reported by, for example, Rudnick et al. (2003), Alford (2003), and Althaus et al. (2003) at most locations but are somewhat closer to Alford's (2003) U.S. East Coast values. Since the cited values are for the tidal and inertial bands the comparison may be somewhat misleading. Nevertheless, inertial and tidal frequency internal waves are primary sources of energy for the high-frequency waves (e.g., Holloway et al. 1997).

An estimate of group speed of a dominant wave packet can be estimated from the ratio of energy flux to total energy (Pedlosky 1979),

$$C_g = \frac{\hat{\mathbf{F}}_h}{\rho_0 \hat{E}}, \tag{5}$$

where the caret implies integration over the water column. For the relatively large amplitude packet near day 284 for ADCP 2 (Figs. 7b, 8b; the event is marked by an asterisk) we find that $C_g = 0.36$ m s^{-1} (0.37 for the secondary N profile); C_g for a first-normal-mode internal wave with period 20 min (the period of the packet occurring at between times 284.1 and 284.2), for N^2 used in the ADCP 2 energy and flux calculations, is about 0.5 m s^{-1}. These speeds are similar to those found by Colosi et al. (2001) for the outer New England shelf.

5. Conclusions

High-frequency (0.5–7.5 cph) internal waves measured with ADCPs moored on the outer New Jersey shelf have depth-averaged baroclinic kinetic and potential energies that are nearly equal and of order 10^{-3} J kg^{-1}. Baroclinic energy flux is found to be nearly horizontal and directed principally to the northwest, upslope relative to local bathymetry. Mean profiles of energy flux are consistent with a dominant first vertical mode. Mean, depth average fluxes are different at the three mooring locations; the difference between ADCP 2 and ADCP 3, which lie along the principal propagation direction, suggests a bulk dissipation of internal-wave energy of about 2×10^{-9} W kg^{-1}. However, the calculated dissipation is probably not a robust result, but it suggests further work with a more complete dataset. In particular, closer spacing of moorings and longer-term salinity–temperature chain moorings would significantly reduce uncertainty. Also, the relatively coarse temporal sampling (for internal-wave periods) should be improved. In future studies, an interval no longer than 1 min should be used. Wave-packet group velocity can be estimated directly from the calculated energies and energy flux. Closer spacing of moored sensors would allow coherent measurement of waveforms, allowing direct determination of phase and group velocities to compare with those indirectly estimated. As an example, a large-amplitude packet yields 0.36 m s^{-1}, comparable to group velocity based on linear wave theory. Using the described methods a number of additional studies are possible. For example, individual events (wave packets) can be analyzed in detail for modal content and propagation characteristics.

Acknowledgments. Ray Burge, Chris Hulbert, Mark Hulbert, and Dan Kennedy of NRL prepared, deployed, and recovered instrumentation used in this study. The authors appreciate the many excellent comments made by the reviewers. This work was supported by the Office of Naval Research under Program PE62435N. We also thank Bill Teague and David Walsh for their help.

REFERENCES

Alford, M. H., 2003: Redistribution of energy available for ocean mixing by long-range propagation of internal waves. *Nature*, **423,** 159–162.

Althaus, A. M., E. Kunze, and T. B. Sanford, 2003: Internal tide

radiation from Mendocino Escarpment. *J. Phys. Oceanogr.,* **33,** 1510–1527.

Apel, J. R., and Coauthors, 1997: An overview of the SWARM shallow-water internal wave acoustic scattering experiment. *IEEE J. Oceanic Eng.,* **22** (3), 465–500.

Baines, P. G., 1982: On internal tide generation models. *Deep-Sea Res.,* **29** (3A), 307–338.

Colosi, J. A., R. C. Beardsley, J. F. Lynch, G. Gawarkiewizc, C.-S. Chiu, and A. Scotti, 2001: Observations of nonlinear waves on the outer New England continental shelf during the summer Shelfbreak Primer study. *J. Geophys. Res.*, **106** (C5), 9587–9601.

Hallock, Z. R., J. Small, J. George, R. L. Field, and J. C. Scott, 2000: Shoreward propagation of internal waves at the Malin shelf edge. *Cont. Shelf Res.,* **20,** 2045–2057.

Holloway, P. E., 1987: Internal hydraulic jumps and solitons at a shelf break region on the Australian North West shelf. *J. Geophys. Res.,* **92** (C5), 5405–5416.

——, P. G. Chatwin, and P. Craig, 2001: Internal tide observations from the Australian North West shelf in summer 1995. *J. Phys. Oceanogr.,* **31,** 1182–1199.

——, E. Pelinovsky, T. Talipova, and B. Barnes, 1997: A nonlinear model of internal tide transformation on the Australian North West shelf. *J. Phys. Oceanogr.,* **27,** 871–896.

Holt, J. T., and S. A. Thorpe, 1998: The propagation of high frequency internal waves in the Celtic Sea. *Deep-Sea Res.*, **44** (12), 2087–2116.

Inall, M. E., G. I. Shapiro, and T. J. Sherwin, 2001: Mass transport by non-linear internal waves on the Malin shelf. *Cont. Shelf Res.,* **21,** 1449–1472.

Kunze, E., L. K. Rosenfeld, G. S. Carter, and M. C. Gregg, 2001: Internal waves in Monterey Submarine Canyon. *J. Phys. Oceanogr.,* **32,** 1890–1913.

MacKinnon, J. A., and M. C. Gregg, 2002: Shear and baroclinic energy flux on the summer New England shelf. *J. Phys. Oceanogr.,* **33,** 1462–1475.

Ostrovsky, L. A., and Y. A. Stepanyants, 1989: Do internal solitons exist in the ocean? *Rev. Geophys.,* **27,** 293–309.

Pedlosky, J., 1979: *Geophysical Fluid Dynamics.* Springer-Verlag, 624 pp.

Phillips, O. M., 1977: *The Dynamics of the Upper Ocean.* Cambridge University Press, 336 pp.

Rudnick, D. L., and Coauthors, 2003: From tides to mixing along the Hawaiian Ridge. *Science,* **301,** 355–357.

Small J., G. Pavey, Z. Hallock, and J. Scott, 1999: Remote sensing and modeling of periodic internal waves at the Malin shelf edge during SES and SESAME 1995: A preliminary investigation. *Cont. Shelf Res.,* **19** (11), 1389–1436.